Microfluidic Immersion Freezing of Binary Mineral Mixtures Containing Microcline, Montmorillonite, or Quartz

Nadia Shardt[1,2]*, Florin N. Isenrich[3], Julia Nette[3], Christopher Dreimol[4,5], Ning Ma[6], Zamin A. Kanji[1], Andrew J. deMello[3], Claudia Marcolli[1]*

[1]Institute for Atmospheric and Climate Science, ETH Zurich, Zürich, 8092, Switzerland

[2]Department of Chemical Engineering, Norwegian University of Science and Technology (NTNU), Trondheim, 7491, Norway

[3]Institute for Chemical and Bioengineering, ETH Zurich, Zürich, 8093, Switzerland

[4]Wood Materials Science, Institute for Building Materials, ETH Zurich, Zürich, 8093 Switzerland

[5]Cellulose & Wood Materials Laboratory, Empa – Swiss Federal Laboratories for Materials Science and Technology, Dübendorf, 8600 Switzerland

[6]Institute for Geochemistry and Petrology, ETH Zurich, Zürich, 8092, Switzerland

Correspondence to: Nadia Shardt (nadia.shardt@ntnu.no) and Claudia Marcolli claudia.marcolli@env.ethz.ch

1 **Abstract**

2 Mineral dusts are among the most active ice-nucleating particles present in cloud droplets, with their

3 properties influencing radiative properties and precipitation formation. To improve weather predictions

4 and climate projections, it is important to understand under which conditions ice will form on mineral

5 dusts. Laboratory experiments have primarily focused on single minerals, and field samples are complex

6 mixtures that cannot be controlled in their composition or particle size. To fill this gap, a bottom-up

7 investigation of suspensions containing pure or binary mixtures of microcline, montmorillonite, or

8 quartz at concentrations between 0.0001 and 0.1 wt.% is presented. Arrays of monodisperse aqueous

9 droplets (diameters of 75 μm) are generated using a microfluidic device and subsequently cooled at a

10 rate of 1 K min^{-1}. The probability of freezing in the presence of binary mixtures generally follows that

11 of the most ice-active mineral. Each pure mineral's nucleation site density is fit as a function of

12 temperature and used to predict the frozen fraction curves for each binary mixture assuming additivity

13 of mineral surface area. Predictions are also made for Arizona Test Dust from the obtained pure mineral

14 fits, and general agreement with experiments is observed. This work presents a systematic study of ice

15 formation in the presence of pure and binary mixtures of common mineral dusts, providing information

16 for the future design of composition-aware parameterizations for ice nucleation in the atmosphere.
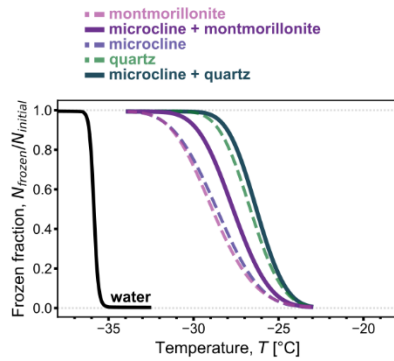
1 Introduction

Heterogeneous ice nucleation in the atmosphere is an important step in the Earth's hydrological cycle, including cloud formation and precipitation. It occurs on ice-nucleating particles (INPs) that are aerosolized primarily from natural sources, of which mineral dust particles have been identified as a significant category both in terms of mass and propensity to catalyze ice nucleation (Beall et al., 2022; Kanji et al., 2017). Other INP types originate from biological and anthropogenic sources (Kanji et al., 2017). INPs are required for the formation of mixed-phase clouds, which contain both liquid water droplets and ice crystals, through a mechanism known as immersion freezing (Vali et al., 2015), wherein INPs immersed in water droplets provide a surface on which ice nucleates upon reaching a sufficiently low temperature. The size and composition of the INP present in a droplet influence the likelihood of ice nucleation. As a consequence, these INP properties affect the properties of mixed-phase clouds since the nucleation of ice precedes many processes that determine what fraction of the cloud becomes ice, such as secondary ice production, collision–coalescence, and the Wegener–Bergeron–Findeisen process (Wegener, 1911; Bergeron, 1935; Findeisen, 1938). Since there are large uncertainties in INP properties, their global distribution, and interactions with other aerosols (such as those of biological origin (Kanji et al., 2017; Klumpp et al., 2022)), the indirect effect of INPs through aerosol–cloud interactions on the Earth's top-of-atmosphere radiative budget remains poorly constrained (Kok et al., 2023).

Numerous studies have reported the ice-nucleating ability of minerals in the immersion mode of freezing, both in the field and in the laboratory. In the field, aerosol samples are characterized using either a continuous flow instrument (e.g., a horizontal ice nucleation chamber (HINC) (Lacher et al., 2017; Rogers, 1988; Rogers et al., 2001)) or a batch assay (e.g., droplet assays (Miller et al., 2021; Wright and Petters, 2013; Polen et al., 2018; Whale et al., 2017)) to quantify the number of freezing events. However, the rarity of ice-nucleating particles in the atmosphere is one challenge for their systematic investigation (Burrows et al., 2022), and it is difficult to draw generalizable conclusions from field campaigns due to a lack of systematic control or knowledge of particle size and composition. Laboratory investigations of single minerals often approach the quantification of ice nucleation behavior in a bottom-up manner: a mineral rock of known composition is crushed, suspended in an aqueous solution, and cooled under observation until ice forms. Such laboratory measurements have been carried out for a range of droplet numbers (tens to thousands) and volumes (microliters to picoliters) (e.g., Atkinson et al. (2013); Tarn et al. (2018); Reicher et al. (2018); House and Dutcher (2024); see Table 1 in Miller et al. (2021) for an overview of instruments reported in the literature), and parameterizations of the observed trends in ice nucleation have been developed for input to climate models.

There has been growing interest in developing parameterizations of ice nucleation that account for the properties of INPs, including their composition and size distribution (Burrows et al., 2022; Chatziparaschos et al., 2023; Knopf and Alpert, 2023). With such an aerosol-aware parameterization (Burrows et al., 2022), the effect of variations in regional emissions might be more accurately accounted for in global models. Presently, primarily single-component, monodisperse aerosols are used as a representative of the true aerosol population. For example, the ice nucleation activity of K-feldspar is an adequate surrogate of mineral dusts (e.g., Atkinson et al. (2013)). Recently, Chatziparaschos et al. (2023) performed simulations using a global chemistry transport model and considered two of the components in the dust, K-feldspar and quartz, to be ice-nucleating. They showed that both mineral types could contribute significantly to ice nucleation depending on their relative concentration and regional temperature, even though K-feldspar is known to initiate ice formation at higher temperatures than quartz. For example, when the mass of quartz was 6 times that of the feldspar, the percentage of ice crystals that formed on quartz particles reached more than 35% (Chatziparaschos et al., 2023).

Wong (2019) investigated one concentration of each of three minerals (0.5 wt.% K-feldspar, 1 wt.% NX illite, and 1 wt.% kaolinite KGa-1b) suspended in binary combinations in water droplets with volumes of 0.2 μL. In this study, the frozen fraction observed in binary mixtures reflected the freezing behavior of the most ice-active single component. However, the concentrations of all combinations of two components were either equal or within a factor of 2, and it was not possible to discern whether there may be a departure from the freezing being dominated by the most active mineral type when the difference in concentrations is much larger, such as the factor of 6 considered in the study by Chatziparaschos et al. (2023).

In this work, we investigate the effect of mineral mixture composition by suspending known concentrations of mineral dust particles in microfluidically-generated aqueous droplets. Both single- and multi-mineral systems are analyzed at varying concentrations (0.0001 to 0.1 wt.% in increments of 10x) of microcline, quartz, and montmorillonite, which have all been identified as important ice-nucleating particles in the atmosphere (Harrison et al., 2019; Harrison et al., 2016; Atkinson et al., 2013). These three minerals are also the primary components of Arizona Test Dust (ATD), a common proxy of atmospheric mineral dust, suspensions of which are also studied herein. A comparison between the ice nucleation activity of the controlled mixtures and that of ATD is drawn to investigate whether samples mixed from the pure components can explain the ice nucleation activity of samples that were collected as mixtures from the air or ground. Through these results, we quantify the likelihood of ice nucleation in binary mineral mixtures, with this information providing a basis for inferring the behavior of immersion mode freezing on real mineral dust mixtures in the atmosphere where concentrations of minerals may span several orders of magnitude.

2 Materials & Methods

For all studied suspensions, we used ultrapure water (molecular biology reagent-grade, Sigma-Aldrich, USA). Single minerals included microcline (originally from Macedonia and obtained from the ETH Mineralogical and Petrographical Collection; milled with a tungsten carbide disk mill), quartz (Sigma-Aldrich, $\geq$ 99.995% trace metals basis), and Na-rich SWy-2 montmorillonite (The Clay Minerals Society). The composition of the microcline and montmorillonite samples were confirmed by powder X-ray diffraction to be 97 % microcline and 3 % albite for the microcline sample (**Fig. A1**), while the montmorillonite sample was pure montmorillonite. Ultrafine Arizona Test Dust (ISO 12103-1, A1 Ultrafine; Filter & Aerosol Technologie GmbH) was used as received, with a documented size distribution of 65.0–69.0 % being less than 5.50 μm in size and 95.5–97.5 % of particles being less than 11 μm.

2.1 Sample Preparation, Droplet Generation, and Cooling

All single minerals (microcline, quartz, and montmorillonite) were suspended in water, sonicated (8 × 30 s pulse in a UP200ST ultrasonic VialTweeter; Hielscher Ultrasonics GmbH, Germany), filtered through a 0.45 μm polyethersulfone sterile syringe filter (TPP Techno Plastic Products AG, Switzerland), dried (SpeedVac, Savant™ SPD111V, Thermo Scientific™, USA), and stored in dried form in separate Eppendorf tubes. On the day of each experiment, a dried sample was resuspended in water and diluted or mixed to the desired concentration. For each pure mineral suspension of 0.1 wt.%, 1 μl was placed on a silicon wafer for SEM analysis. Immediately before generating droplets, the resuspended sample was transferred to the polytetrafluoroethylene (PTFE) tubing attached to the syringes and pumps for controlling the sample flow rate. For samples of ATD, dust was only suspended in water and sonicated (VialTweeter) without filtration or further drying, followed by physical agitation (shaking) immediately prior to being transferred to the PTFE tubing before droplet generation. To remove the possibility for contamination in the inlet PTFE tubing to the microfluidic device, the same tubing was only reused for experiments with the same mineral. The tubing was also flushed with isopropanol after each day of experiments. If multiple mineral concentrations were investigated on the same day, the lower concentration of each mineral suspension was investigated first to avoid potential contamination of subsequent experiments.

Three independent populations of droplets were generated sequentially from the same starting suspension in the Microfluidic Ice Nuclei Counter Zürich (MINCZ) (Isenrich et al., 2022). MINCZ consists of: a polydimethylsiloxane (PDMS) microfluidic device, three glass syringes (1 mL, Hamilton® syringe, Sigma-Aldrich) in syringe pumps (Aladdin AL1000-220Z, World Precision Instruments, USA), high-purity perfluoroalkoxyalkane (PFA) tubing (50 cm in length with 360 μm o.d. and 75 μm i.d.; IDEX Health & Science LLC, USA) to store the generated droplets, a stereoscope

(Nikon SMZ1270, 0.5× objective lens, fibre ring illuminator with LED light source), a CMOS camera (iDS UI-3060CP-M-GL Rev. 2) for optical freezing detection, and cooling instrumentation (an ethanol bath cooled by a Peltier element (PKE 128A 0020 HR 150, Peltron GmbH, Germany) and a chiller (Huber KISS K6, Huber Kältemaschinenbau AG, Germany) that recirculates an aqueous 55% v/v ethylene glycol (98% technical grade, Sigma-Aldrich, USA) solution). PDMS microfluidic devices were manufactured following an established protocol, as described by Isenrich et al. (2022). Briefly, this involved patterning of an SU-8 coated silicon wafer, transferring this pattern to PDMS (Elastosil RT 601 A/B, Ameba AG, Switzerland; mass ratio of 10:1 between the base and curing agent) via soft lithography and bonded the structured PDMS layer to a glass slide (Menzler-Glaser, Germany) via plasma treatment. Using MINCZ, 75-μm diameter aqueous droplets were generated within a continuous surfactant laden oil phase (1% v/v 008-FluoroSurfactant–RAN Biotechnologies, USA in HFE-7500) and stored in the PFA tubing, followed by cooling at 1 K min^{-1} (automatically controlled by a proportional controller implemented in Python with images saved every 3 s). As discussed by Alpert & Knopf (2016), a sufficient number of experiments and number of droplets are needed for a reliable statistical interpretation of heterogeneous nucleation. Based on these recommendations around 100–200 droplets and three repeats were used for experiments in the current study. There were inherent variations in the number of droplets observed in each experiment because of variability in the process of droplet generation between experiments. The primary goal of droplet generation was to obtain a stable, monodisperse population of droplets with sufficient spacing to avoid droplet coalescence. The spacing proved to be slightly variable depending on the exact fluid flow rates required to achieve a stable droplet population, which influenced the number of droplets in the field of view.

2.2 Mineral Characterization

Secondary electron scanning electron microscopy (SEM) images were obtained using a FEI Magellan 400 scanning electron microscope. Each pure mineral was pre-processed (sonication, filtration, and drying) and re-suspended in a 0.1 wt.% aqueous solution. A single droplet of this suspension was deposited on a dried and ultrasonicated silicon substrate for characterization.

Dynamic vapor sorption (DVS; Advantage ET 1, Surface Measurement Systems Ltd., London, UK) using deionized water was employed to measure the adsorption isotherms. Samples were preconditioned at 298 K for 720 min under a nitrogen atmosphere (grade N5.0) to remove any pre-adsorbed moisture. Subsequently, samples were subjected to stepwise increases in relative humidity (RH), with increments of 5 % RH between 0 %–40 %, 10 % RH between 40 %–70 %, and 2 % RH between 70 %–98 %. Quasi-equilibrium at each step was defined as a mass change rate below 0.0005 % min^{-1} over a period of 10 min, or after a maximum duration of 1000 min. Throughout the experiment, the temperature was maintained at 298 K, while nitrogen (grade N5.0) served as the carrier gas at a constant flow rate of 200 mL min^{-1} to regulate RH. The specific surface area (A_s; m²/g) of the

solid particles was estimated in accordance with the Brunauer–Emmett–Teller (BET) model, consistent with previous studies (Gronquist et al., 2019; Klumpp et al., 2023; Mahrt et al., 2023). For this purpose, data points from the adsorption isotherms within the 15 %–35 % RH range were used to perform a linear regression. A cross-sectional area of 0.114 nm² per water molecule was assumed to represent monolayer coverage.

Based on the observed fraction of frozen droplets during an experiment as a function of temperature ($N_{\text{frozen}}/N_{\text{total}}$), the number of nucleation sites per unit surface area, n_s, was calculated using (Vali, 2014)

$$n_s = -\frac{\ln\left(1 - \dfrac{N_{\text{frozen}}}{N_{\text{total}}}\right)}{A} \tag{1}$$

where $A = A_s m w_i$ and m is the mass of a droplet (221 ng) and w_i is the mineral mass fraction in a droplet.

2.3 Image Analysis

Automated detection of possible freezing events (**Fig. 1**) was carried out in three steps. In Step 1, the location of the PFA tubing in each recorded image was detected using an algorithm developed by Deck et al. (2024), consisting of histogram equalization, Otsu's thresholding, and smoothing with a Savitzky–Golay filter. For one experimental series, the raw recorded image sequences were not completely stationary, so image registration (i.e., image alignment) was carried out by identifying features, tracking their evolution over time, and aligning the images accordingly (using the scikit-image package in Python) before carrying out further analysis. In Step 2, the difference image between two consecutive images was calculated (I_t and $I_{t-\Delta t}$), and in Step 3, the OpenCV package in Python was used for further image processing (1936×1216 pixels) aimed at identification of potential freezing events through a sequence of steps: bilateral filtering, opening, Canny edge detection, Hough circle detection, and applying a threshold for the average greyscale value within the found circles. Each potential freezing event was cropped to an image size of 60×60 pixels and passed to classification by a deep convolutional neural network (CNN).
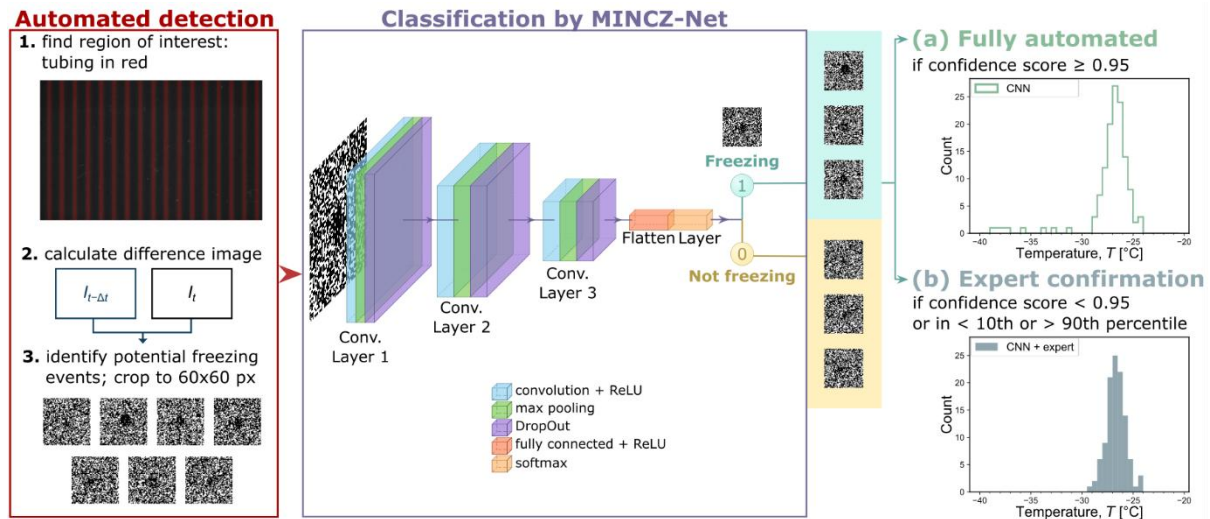
Figure 1. Image processing workflow consisting of automated detection of potential freezing events and a convolutional neural network, MINCZ-Net, for their classification to obtain either (a) a fully automated count of frozen droplets as a function of temperature or (b) a count that is confirmed by the expert.

At the classification stage, the CNN named MINCZ-Net was used to classify each event as either "freezing" or "not freezing". The CNN contained three sets of convolutional, pooling, and dropout layers (as shown in **Fig. 1**; implemented with the TensorFlow and Keras packages in Python) between the input and output layers, and it was trained on images from three experiments (one from each pure mineral suspension) for a total of 689 images with an 80:20 split between training and test data. The last layer used rectified linear unit (ReLU) and softmax activation functions to determine the final classification. In the fully automated workflow (**Fig. 1a**), freezing events identified with a confidence score $\geq$ 0.95 were counted as a function of temperature. In comparison, the workflow with expert confirmation (**Fig. 1b**) prompted the expert to assess any freezing events that were classified by MINCZ-Net with a confidence score < 0.95 and those that were below the 10th percentile or above the 90th percentile of the population.

Since the neural network training was carried out for one experiment for each single mineral, we tested the accuracy of the resulting classification for five other cases—one for each binary mineral mixture containing microcline (mc), quartz (qu), and montmorillonite (mm), as shown in **Fig. 2**. Results from three methods of classifying potential freezing events are shown: by the expert only, fully automated by the CNN (**Fig. 1a**), and with expert confirmation of the CNN categorization (**Fig. 1b**). All three methods yielded similar counts of freezing events as a function of temperature. The most important difference is in the tails of the frozen fraction distribution, where the expert alone and the combined CNN–expert methods identified fewer freezing events than the CNN alone. False positives may occur with the CNN due to noise or optical interference (e.g., dust moving in between frames) resembling a freezing event with a localized increase in pixel brightness, and thus the CNN method overestimates

1 the number of freezing events. The expert-only method generally identifies more freezing events than
2 the combined CNN–expert method due to the false negative categorizations by the CNN; other
3 deviations between these methods can also originate from expert classification error. Between the
4 expert-only and the CNN–expert methods, the CNN–expert analysis is beneficial when considering the
5 required analysis time for one experiment (up to 1000 potential freezing events): more than 1 h is needed
6 to classify all the possible freezing events by an expert alone, while less than 15 min is typical for the
7 CNN and expert together. Thus, the best methodology for counting the number of frozen droplets is a
8 combination of the CNN with expert confirmation, and this is used in all experiments.
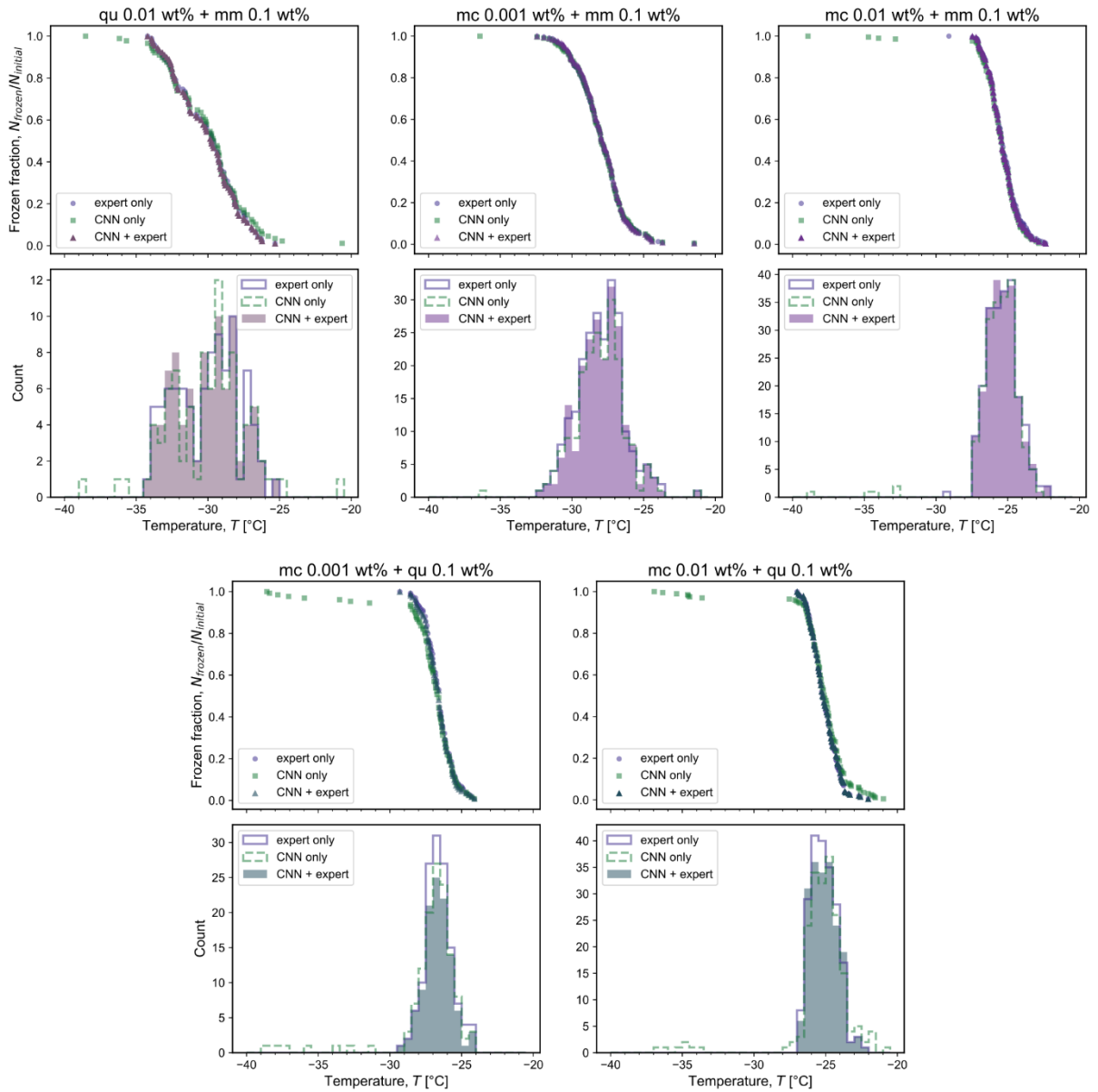
11 **Figure 2.** Comparison of frozen fraction and counts of freezing events for one experiment on each mineral mixture containing
12 quartz (qu), montmorillonite (mm), or microcline (mc) of different weight percentages. The results were obtained through
13 classification by the expert only (purple circles and line); the convolutional neural network (CNN) (green circles and dashed
14 line); and the CNN followed by expert confirmation (triangles and shaded region) of the frozen droplets that were classified

with either less than 95% confidence by the CNN or were below the 10th percentile or above the 90th percentile. The total number of droplets present in the field of view is assumed to be equal to the total number of freezing events detected, with variations between experiments arising from differences in droplet spacing during droplet generation.

2.4 Governing Equations for Fitting and Prediction

The following empirical equation was fit to the experimentally-derived n_s values as a function of temperature for each pure mineral:

$$n_{s,i} = 10^{a_i}[-b_i(T - c_i)]^{d_i} \tag{2}$$

where a_i, b_i, c_i, and d_i are fitting coefficients for mineral i determined after discarding the first 10 % of data points calculated from the experimental frozen fraction to prevent overfitting to the rare nucleation events at the higher temperatures. The curve_fit function in the Python package SciPy was used for obtaining fitting coefficients that minimized the sum of squares of residuals. For all coefficients reported herein for Eq. (2), T is in units of °C and n_s is in units of cm^{-2}. The goodness of fit was assessed via the standard deviation (SD) calculated using:

$$SD = \sqrt{\frac{\sum_i^n \left(\log_{10} \hat{n}_{s,i} - \log_{10} n_{s,i}\right)^2}{N - p}} \tag{3}$$

where $\hat{n}_{s,i}$ is a predicted value, $n_{s,i}$ is an experimental value, N is the number of experimental data points, and p is the number of fitting parameters ($p = 4$). The validity of the obtained fit is limited to the range of experimental temperatures, and the expression should be used with caution outside this range.

Using the pure mineral fits for n_s, predictions of frozen fraction for mixtures as a function of temperature were calculated by applying Eq. (1) to a multi-mineral suspension where $n_s A = \sum_i n_{s,i} A_i$ to yield the following expression:

$$\frac{N_{\text{frozen}}}{N_{\text{total}}} = 1 - \exp\left(-\sum_i n_{s,i} A_i\right) \tag{4}$$

where $A_i = A_{s,i} m w_i$.

3   Results and Discussion

3.1 Freezing Temperatures of Pure Mineral Suspensions

The observed frozen fractions of droplets as a function of temperature are shown in **Fig. 3** (symbols) with each frozen fraction calculated as the ratio between the number of frozen droplets and the total number of droplets in an experiment. The relative ability of each pure mineral to nucleate ice is comparable to previous reports, with microcline being the most ice-active mineral at the highest temperature (Atkinson et al., 2013; Harrison et al., 2019), followed by quartz and montmorillonite (Atkinson et al., 2013; Harrison et al., 2019; Pinti et al., 2012), although a wide variety in activity has also been reported depending on the source of the mineral (Kanji et al., 2017; Harrison et al., 2016; Hoose and Möhler, 2012; Murray et al., 2012; Harrison et al., 2019). For each series of experiments in **Fig. 3**, the temperature at which nucleation is observed decreased as the concentration of the mineral in each droplet decreased. This is expected because the surface area available for ice nucleation decreases with reducing concentration, thus lessening the probability of ice nucleation. **Fig. 3** also presents the homogeneous freezing of contemporaneously-measured pure water droplets (black circles and light grey shading) from Isenrich et al. (2022), confirming that droplets with higher mineral concentrations freeze at higher temperatures than the pure water background.
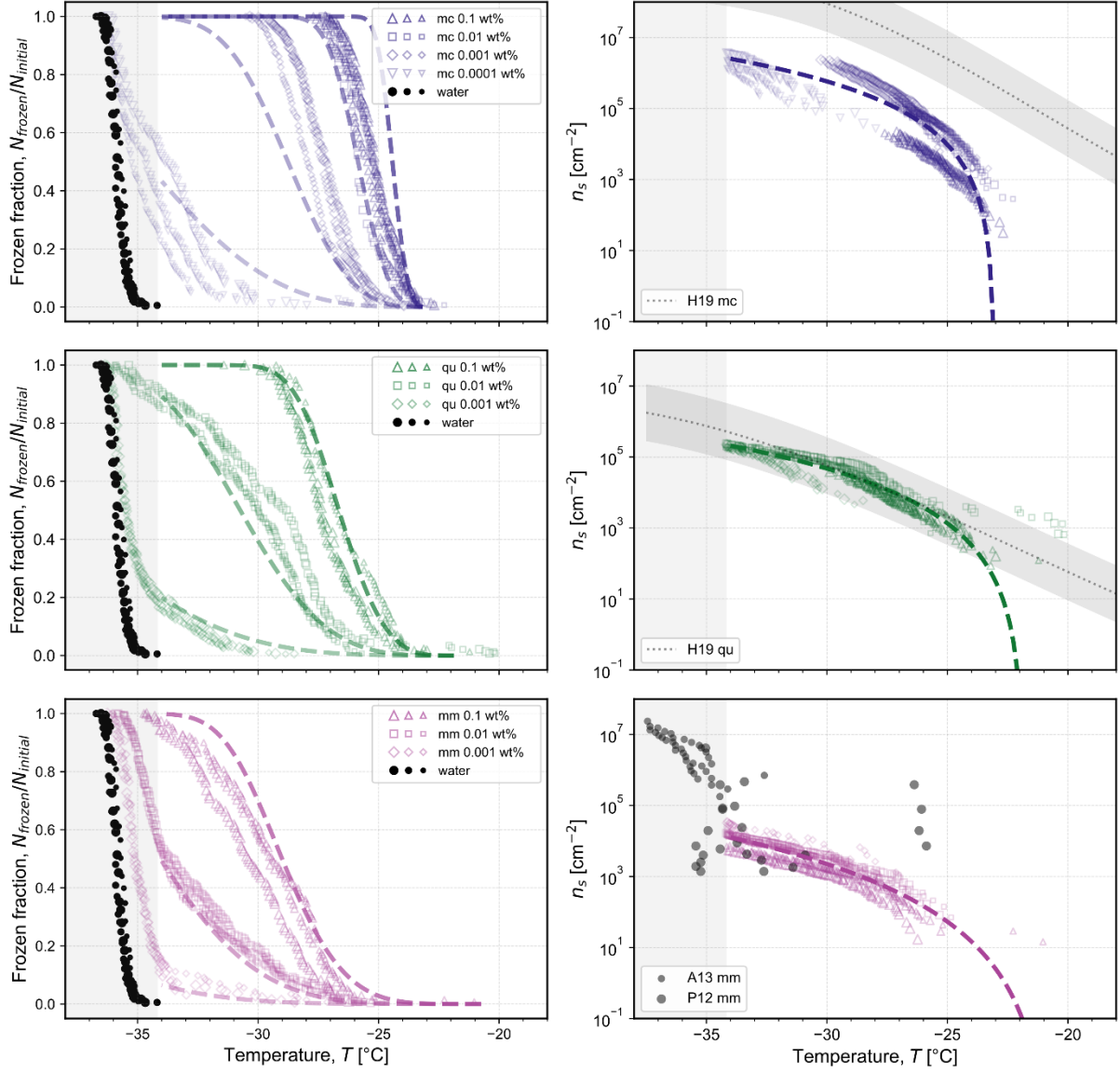
Figure 3. Frozen fraction of droplets as a function of temperature for each studied single mineral: microcline (mc) at concentrations of 0.1, 0.01, 0.001, and 0.0001 wt.%; quartz (qu) at concentrations of 0.1, 0.01, and 0.001 wt.%; and montmorillonite (mm) at concentrations of 0.1, 0.01, and 0.001 wt.%. The measured frozen fraction for the homogeneous freezing of water droplets of the same volume shown with black symbols is reproduced from Isenrich et al. (2022). Each symbol type denotes a different mineral concentration, and the different symbol sizes represent independent populations (i.e., triplicates) of monodisperse droplets with diameters of approximately 75 μm cooled at 1 K min⁻¹ (temperature uncertainty is 0.2 K (Isenrich et al., 2022)). The corresponding number of nucleation sites per unit surface area, n_s, is plotted as a function of temperature according to Eq. (1) using specific surface areas of 102 m²/g, 48 m²/g, and 241 m²/g for mc, qu, and mm, respectively. For comparison, parameterizations or experimental data of n_s are plotted and labeled as: H19 from Figure 7 in Harrison et al. (2019) with shading for the reported uncertainty; A13 from Atkinson et al. (2013); and P12 from Pinti et al. (2012) as calculated by Hoose and Möhler (2012). The dashed lines are model fits for n_s as a function of temperature, from which frozen fraction curves are calculated using Eq. (1). The equations are given by: $n_{s,\mathrm{mc}} = 10^{2.3344}[-1.6598(T + 23.054)]^{3.2291}$, $n_{s,\mathrm{qu}} = 10^{0.8924}[-1.2756(T + 21.865)]^{3.7223}$, and $n_{s,\mathrm{mm}} = 10^{-0.2189}[-0.5956(T + 20.744)]^{4.8178}$. In all plots, the shaded grey area at the lowest temperatures highlights the region where the homogeneous nucleation of pure water in 75 μm droplets occurs; n_s values are thus not plotted in this region.

Figure 3 also shows the number of nucleation sites per unit surface area, n_s, for temperatures above the onset of homogeneous freezing. Eq. (1) was used with $A_s = 102$, 48, and 241 m^2/g for microcline, quartz, and montmorillonite, respectively, as obtained from BET analysis of DVS measurements (shown in **Fig. 4** alongside SEM images) to convert experimental frozen fractions to n_s vs. T. For microcline and montmorillonite, the derived n_s values do not agree between different mineral concentrations, which suggests that there are differences in the number of nucleation sites per unit surface area as a function of concentration. However, we cannot exclude the possibility that these apparent discrepancies may be due to deviations in the actual suspension concentrations from the nominal ones in the process of preparing the samples from the stock suspension. To obtain a representative model of the site density, we therefore consider all n_s data over all mineral concentrations of a single mineral. The dashed lines in the plots of n_s in **Fig. 3** are fits obtained using Eq. (2) for microcline, quartz, and montmorillonite with standard deviations (SD) for $\log_{10} n_s$ of 0.47, 0.19, and 0.22, respectively. The highest standard deviation is obtained for microcline due to the spread of the experimentally-derived values of n_s between different nominal suspension concentrations. The obtained fitting parameters for each pure mineral were used to calculate frozen fractions for each concentration using Eq. (1), as illustrated by dashed lines in **Fig. 3**, showing close agreement with experimental observations for quartz and montmorillonite. Some of the predicted frozen fractions for microcline, however, deviate from those obtained experimentally, with a steeper slope in frozen fraction predicted for the highest concentration of 0.1 wt.% and a shallower slope for the concentration of 0.001 wt.%. As in our analysis of n_s for microcline, we attribute these discrepancies to potential variation in the actual concentration of the suspensions. The three replicates shown at each concentration were prepared from the same starting suspension and show high reproducibility, while different concentrations were prepared independently, and variability may be greater.
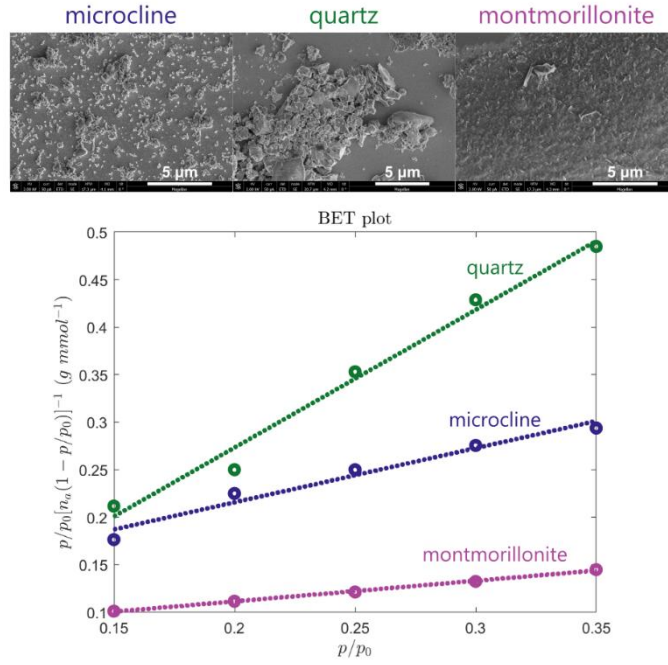
Figure 4. Scanning electron microscopy images and linear regressions performed on adsorption isotherm measurements via dynamic vapor sorption (DVS; see **Fig. A2**) for the determination of the BET surface area of each mineral (microcline, quartz, and montmorillonite) after sonication, filtration, and drying.

Figure 3 includes representative correlations or experimental data from the literature for nucleation site density as a function of temperature for each mineral. It is difficult to draw an exact comparison between our results and literature reports of n_s, since ice activity depends on the exact physicochemical properties of a mineral sample, such as its composition, source, processing (e.g., milling), size, and age. For microcline samples, our results indicate a lower density of nucleation sites compared to literature values (Harrison et al., 2019) by approximately 1–2 orders of magnitude. This may be due to an inherently different ice activity for the sample studied or due to a dependence of ice activity on particle size. We filtered all pure mineral samples through a 0.45 µm filter to narrow the polydispersity of particle sizes between droplets and to reduce the probability of clogging in the microfluidic device; such size selection may influence the resulting ice nucleation behavior if smaller particles have either fewer or inferior active sites. For quartz and montmorillonite samples, our results for n_s as a function of temperature broadly align with the representative literature sources. In Atkinson et al. (2013), a different montmorillonite was investigated (STx-1 containing Ca^{2+}) compared to the one used herein (SWy-2 containing primarily Na^+), and it has previously been reported to be less ice active than SWy-2 (Pinti et al., 2012; Kumar et al., 2023).

Another contributing factor to the different orders of magnitude of n_s for microcline and montmorillonite shown in **Fig. 3** may be the uncertainty in the determination of specific surface area (A_s), both in our work and in previous reports. In the literature, specific surface areas are determined

based either on the BET adsorption of nitrogen or on the particle size distribution observed via SEM imaging. Adsorption-based measurements typically yield higher estimates of A_s because they capture the rough surface features and internal surface area (e.g., pores) of the sample. In addition, BET measurements with water tend to overestimate the surface area compared to the same measurements carried out with nitrogen (Blattmann and Plötze, 2024). The relatively high specific surface areas measured for the studied minerals is partially due to the small particle sizes (filtered through a 0.45 μm filter), but more likely attributed to a significant amount of internal surface area. Assuming a mineral density of $\rho = 2.6$ g/cm^3 and a perfectly spherical particle diameter of $D = 450$ nm yields a specific surface area of $6/\rho D = 5.1$ m^2/g, which is 1–2 orders of magnitude smaller than the estimated BET values. In comparison, for example, reported specific surface areas of montmorillonite samples range between 22.7 and 350 m^2/g (Dogan et al., 2007), with a value of 31.82 m^2/g for SWy-2 (Pinti et al., 2012). For microcline samples, reported BET specific surface areas have typical values of around 2–3 m^2/g (1.91 m^2/g (Kumar et al., 2018); 1.6 m^2/g (Klumpp et al., 2022); 3.2 m^2/g (Atkinson et al., 2013); and 1.8–3 m^2/g (Peckhaus et al., 2016). For quartz, a value of 5.5 m^2/g was previously reported by Zolles et al. (Zolles et al., 2015) in a sample where 80 % of the particles had sizes between 1 and 5 μm. Thus, the combination of smaller particle sizes and significant internal surface area contributes to the difference in the magnitude of the specific surface areas for the pure minerals studied herein compared to the literature.

3.2 Freezing Temperatures of Binary Mineral Mixtures

Three binary mixtures containing microcline, quartz, and montmorillonite are shown in **Fig. 5** in comparison to the pure minerals at the concentrations that comprise the mixture. For both mixtures containing 0.01 wt % microcline (**Fig. 5a** and **5b**), there is no significant difference between the experimental frozen fractions of the mixture and those of the pure microcline (symbols), as expected based on the predictions using Eq. (4) assuming additivity of the pure minerals' surface areas (solid lines). Even though the concentrations of quartz and montmorillonite in their respective binary mixtures are 10x that of microcline, the active sites on quartz and montmorillonite were less active than those of microcline. For the mixture containing 0.01 wt.% quartz and 0.1 wt.% montmorillonite, the frozen fractions follow the same trend as the individual minerals' frozen fraction, which are themselves indistinguishable at these concentrations. Even though there was more surface area available for nucleation to occur in the binary mixture, there was no increase in the observed nucleation temperature, suggesting that the 0.01 wt.% quartz and 0.1 wt.% montmorillonite surfaces do not have a detectable additive effect. This is likely because the available surface area was only doubled, and this change did not lead to a measurable change in the frozen fraction within the variability of replicate experiments, as is shown by the solid line in **Fig. 5c** depicting the frozen fraction calculated using Eq. (4) with the pure

1 quartz and montmorillonite fits of n_s. To detect a significant enough change in the frozen fraction, the

2 available surface area would need to increase by a larger factor, such as that between 0.01 wt.% quartz

3 and 0.1 wt.% quartz leading to the shift in frozen fraction shown in **Fig. 3**.
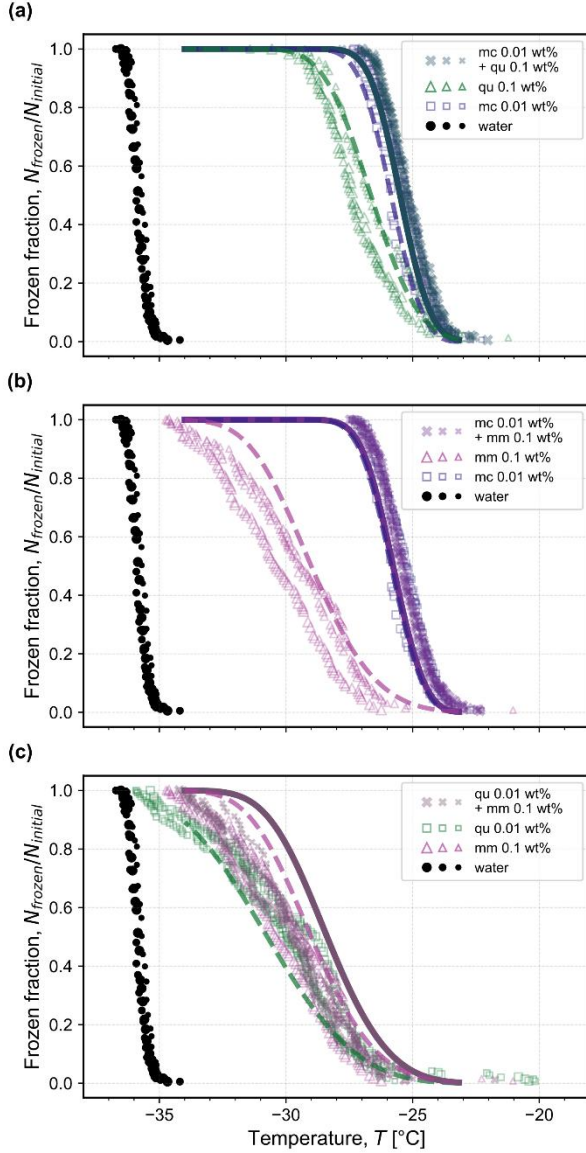
6 **Figure 5.** Frozen fraction of droplets as a function of temperature for three binary mixtures where the most active single

7 mineral dictates the mixture's freezing behavior: (a) 0.01 wt.% microcline (mc) and 0.1 wt.% quartz (qu); (b) 0.01 wt.%

8 microcline and 0.1 wt.% montmorillonite (mm); and (c) 0.01 wt.% quartz and 0.1 wt.% montmorillonite. The constituent

9 single-mineral frozen fractions are reproduced from **Fig. 3** for comparison at the corresponding concentration in each mixture.

10 The measured frozen fraction for the homogeneous freezing of water droplets of the same volume shown with black symbols

11 is reproduced from Isenrich et al. (2022). Each symbol size represents an independent population of monodisperse droplets

12 (i.e., triplicates) with diameters of approximately 75 μm cooled at 1 K min^{-1} (temperature uncertainty is 0.2 K (Isenrich et al.,

13 2022)). Dashed lines are calculated from the pure component fits of n_s vs. T using Eq. (1), and solid lines are predictions (not

14 fits) using Eq. (4) with input of the pure component n_s fits.

When the microcline concentration was decreased from 0.01 wt.% to 0.001 wt.% in the binary mixtures with quartz and montmorillonite, the nucleation temperatures of the droplets decreased accordingly, as shown in **Fig. 6**. In the binary mixture containing microcline and quartz, there is no significant change in the frozen fraction curves compared to the individual minerals' frozen fractions that were observed experimentally (open triangles and diamonds). In the binary mixture containing microcline and montmorillonite, however, there was a significant proportion of droplets freezing in the tail end at even lower temperatures than observed for droplets containing pure microcline. This observation can also be seen by directly comparing the microcline–quartz mixture with the microcline–montmorillonite mixture, as shown in **Fig. 6c**. Here, approximately 15 % of the microcline–montmorillonite droplets froze at temperatures below −30 °C, where there was no observed freezing for the microcline–quartz mixture.
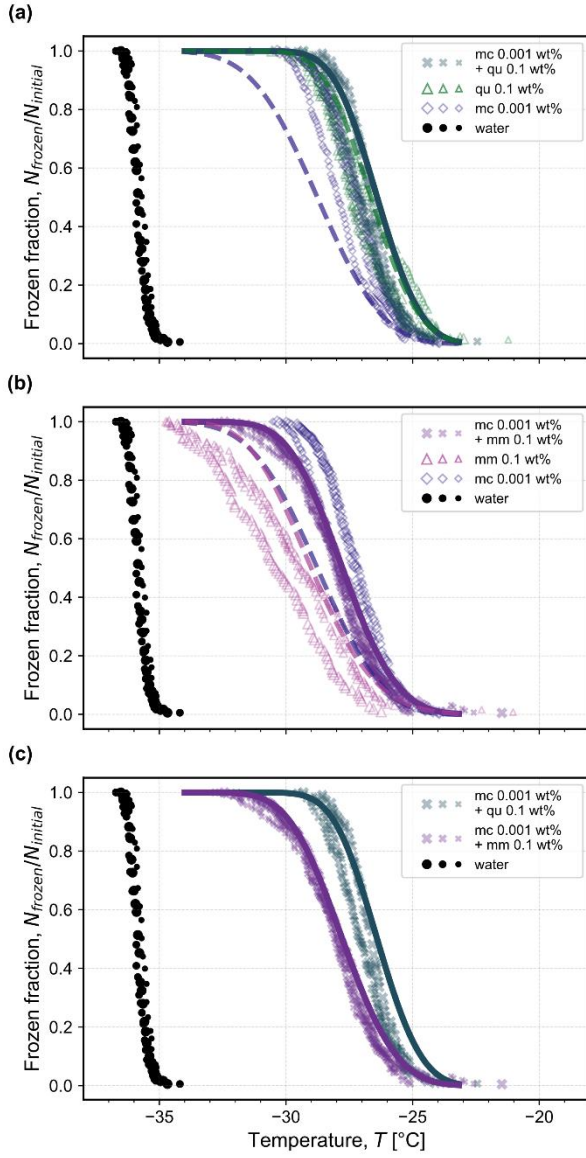
3   **Figure 6.** Frozen fraction of droplets as a function of temperature for two binary mixtures containing 0.001 wt.% microcline

4   (mc) and (a) 0.1 wt.% quartz (qu) or (b) 0.1 wt.% montmorillonite (mm). The constituent single-mineral frozen fractions are

5   reproduced from **Fig. 3** for comparison at the corresponding concentration in each mixture. In (c), the binary mixtures are

6   directly compared to highlight the noticeable reduction in ice nucleation activity in the presence of 0.1 wt.% montmorillonite

7   compared to 0.1 wt.% quartz with the same concentration of 0.001 wt.% microcline. The measured frozen fraction for the

8   homogeneous freezing of water droplets of the same volume shown with black symbols is reproduced from Isenrich et al.

9   (2022). Each symbol size represents an independent population of monodisperse droplets (i.e., triplicates) with diameters of

10   approximately 75 μm cooled at 1 K min^{-1} (temperature uncertainty is 0.2 K (Isenrich et al., 2022)). Dashed lines are calculated

11   from the pure component fits of n_s vs. T using Eq. (1), and solid lines are predictions (not fits) using Eq. (4) with input of the

12   pure component n_s fits.

1 One possible explanation for the extended tail of the distribution could be that the 100x higher

2 concentration of montmorillonite compared to microcline may interfere with the activity of microcline

3 in solution. SWy-2 montmorillonite is a clay mineral that releases Na^+ ions when suspended in water,

4 and we hypothesize that these ions may exchange with the K^+ ions at the surface of the microcline. Such

5 ionic interactions between microcline and dissociated species were hypothesized by Kumar et al. (2018)

6 to explain the enhancement or reduction in the ice-nucleation activity of microcline suspensions

7 containing different combinations of NH_4^+, Na^+, K^+, SO_4^{2-}, Cl^-, and NO_3^-. The presence of any cation

8 except NH_4^+ decreased the ice-nucleation activity of microcline at the studied concentrations. Whale et

9 al. (2018) and Hamzehpour et al. (2022) also reported a reduction in the activity of microcline in the

10 presence of NaCl. In addition, Yun et al. observed a reduction of microcline's ice-nucleation activity in

11 the presence of inorganic acids and carboxylic acids (Yun et al., 2021) and $NaNO_3$ (Yun et al., 2020).

12 It is therefore likely that the surface interaction of microcline with Na^+ ions from montmorillonite

13 explains why the frozen fraction curves of microcline–montmorillonite droplets lie between the frozen

14 fraction curves of the pure minerals at their respective concentrations. In contrast, at the higher

15 concentration of microcline (0.01 wt.%) in the binary mixture with montmorillonite shown in **Fig. 5b**,

16 we hypothesize that the concentration of montmorillonite was insufficient (only 10x higher than

17 microcline) to fully exchange surface ions; there was therefore no perceptible change in the frozen

18 fraction of the mixture compared to that of pure microcline at the same composition.

20 Yet we cannot exclude the possibility that experimental variability in the determination of microcline's

21 ice nucleation activity explains the observed tail of the microcline–montmorillonite mixture compared

22 to the microcline–quartz mixture. As shown in **Fig. 3**, the trend of n_s vs. T for microcline derived from

23 experimental frozen fractions does not collapse onto a single line over all studied concentrations, and

24 in **Fig. 6**, the obtained fit for n_s to this data thus yields a frozen fraction at lower temperatures (dashed

25 blue line) than those observed experimentally at a nominal microcline concentration of 0.001 wt.%

26 (open diamonds). If the true activity of 0.001 wt.% microcline is represented by the dashed blue line,

27 then the frozen fraction observed in **Fig. 6a** for microcline–quartz is explained by the inherent activity

28 of a 0.1 wt.% quartz suspension, and the frozen fraction observed in **Fig. 6b** for microcline–

29 montmorillonite is explained by the additive activity of each constituent, as depicted by the solid purple

30 line calculated using Eq. (4).

32 **Figure 7** highlights the freezing behavior of some studied aqueous suspensions containing pure

33 minerals and their binary mixtures, and all experiments are shown in **Fig. A3**. The corresponding

34 average median temperature T_{50} for each set of three independent experiments at each concentration is

35 also shown. A statistical comparison of all pairs of T_{50} was carried out (**Table A1**), highlighting several

36 significant differences between pure components and the binary mixtures, as shown in **Fig. 7** denoted

37 by asterisks. In mixtures containing microcline at 0.01 wt.%, the median freezing temperature is greater

than that of the second component, whether it is quartz or montmorillonite. As seen previously in **Fig. 6**, we confirm that there is a statistically significant difference (according to Welch's unequal variances *t*-test) between the median freezing temperature of the microcline–quartz and microcline–montmorillonite mixtures when microcline was present at a concentration of 0.001 wt.%. We also confirm that there is no statistically significant difference between the median freezing temperature of the mixture containing microcline at 0.001 wt.% and quartz at 0.1 wt.% when compared to the median freezing temperatures of the pure minerals at the same concentrations (also seen in **Fig. 6**).
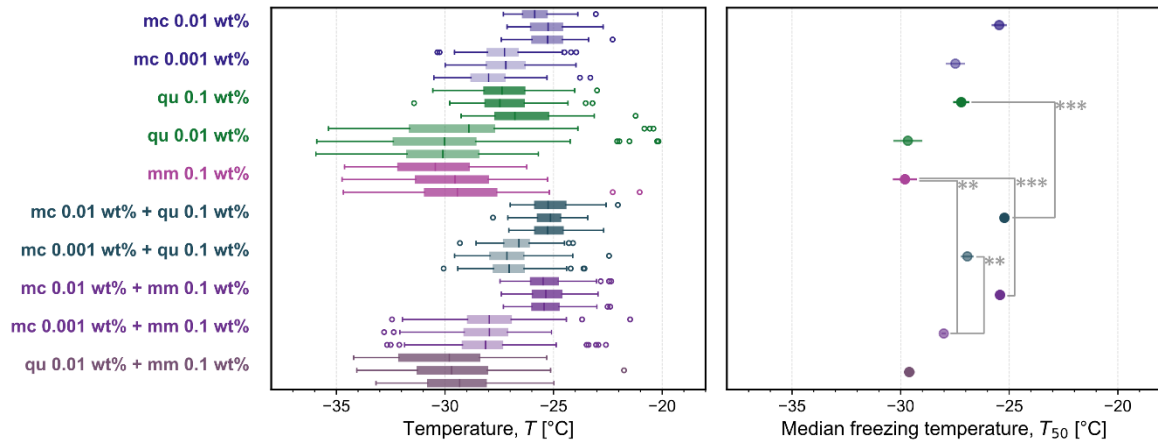
Figure 7. Box plot of the freezing temperatures for a subset of all experiments shown in **Fig. A3**: pure microcline (mc 0.01 and 0.001 wt.%), quartz (qu 0.1 and 0.01 wt.%), montmorillonite (mm 0.1 wt.%), and all studied binary mixtures in triplicate. In each box plot, the vertical line indicates the median freezing temperature, the upper and lower bounds of the box stretch across the 25th to 75th percentiles, whiskers span the maximum and minimum temperatures, and open circles are outliers beyond 1.5 times the interquartile range. The corresponding average median temperature T_{50} is plotted for each set of three experiments (error bars show one standard deviation). Four significant differences in median freezing temperature are labeled with two or three asterisks to denote that Welch's unequal variances *t*-test yielded $p \leq 0.01$ (**) or $p \leq 0.001$ (***).

Figure 7 also shows the relative unimportance of quartz in the quartz–microcline mixtures even when the mass of quartz is ten or a hundred times that of microcline. This is an interesting comparison to the results of Chatziparaschos et al. (2023), who modelled ice nucleation in a global climate model and determined that the percentage of ice crystals forming on quartz particles was more than 35% when the mass of quartz was 6x that of feldspar. This difference may be a result of the droplets herein containing an internal mixture of quartz and microcline instead of each droplet containing either quartz or microcline. In a cloud, each droplet would only contain a single ice-nucleating particle (an external mixture), and thus particles that are less active can still contribute to the frozen fraction, because ice nucleation is not initiated at a higher temperature by the presence of a particle that is more active.

3.3 Freezing Temperatures of Arizona Test Dust (ATD) Suspensions

Figure 8 summarizes the observed frozen fractions and corresponding nucleation site densities for suspensions of ATD at three concentrations (symbols). As expected, the freezing temperatures decreased as the concentration decreased, in line with the decrease in surface area available for freezing. Normalizing based on the surface area through Eq. (1) shows that all results collapse onto a single curve of n_s as a function of temperature. The specific surface area has been shown to vary as a function of particle size; for example, Ibrahim et al. (2018) reported a value of 37.8 ± 1.7 m^2/g for the 0–3 μm nominal size range and a value of 2.8 ± 0.4 m^2/g for the 40–80 μm nominal size range. We assume a specific surface area of 22 m^2/g from Ibrahim et al. (2018) for the fraction of particle sizes between 5 and 10 μm to represent the specific surface area of the A1 Ultrafine ATD investigated herein, which is documented to have 95.5–97.5 % of particles being < 11 μm in size by the supplier. Our results for nucleation site density are lower than representative literature sources (Wheeler et al., 2015; Hader et al., 2014), possibly due to natural variation in the source material or a different assumption for the specific surface area. As reported by Kaufmann et al. (2016), ATD consists primarily of microcline, quartz, and montmorillonite (29 wt.%, 23 wt.%, and 25 wt.%, respectively, for a total of 77 wt.%), while for a sample containing the nominal 0–3 μm fraction analyzed by Broadley et al. (2012), the composition was 33.2 wt.% feldspar and 17.1 wt.% quartz, with 10.2 wt.% being an illite–smectite mixed layer). No individual component is present at concentrations orders-of-magnitude higher than the others, in contrast to the experiments performed for binary mixtures shown in **Fig. 5** and **Fig. 6**. Instead, all three minerals are present in similar proportion, and all provide a comparable surface area for ice nucleation.
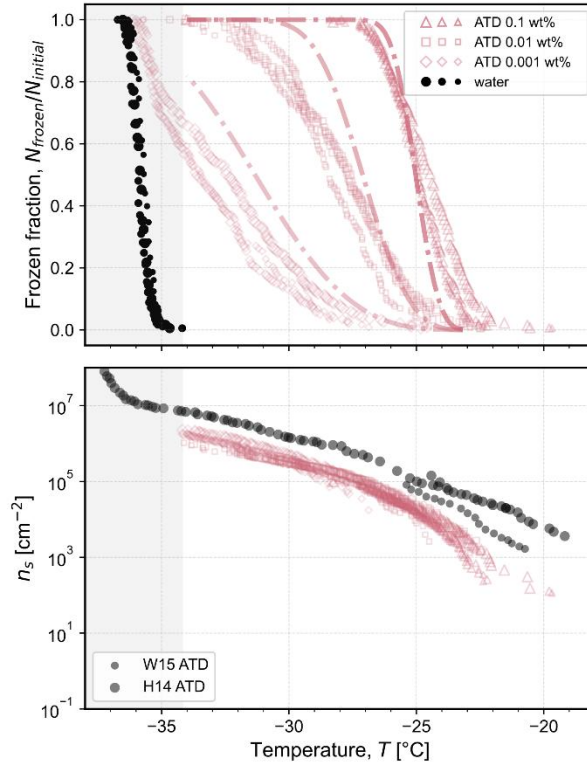
Figure 8. Frozen fraction of droplets as a function of temperature for Arizona Test Dust (ATD; A1 Ultrafine) at concentrations of 0.1, 0.01, and 0.001 wt.%. The measured frozen fraction for the homogeneous freezing of water droplets of the same volume shown with black symbols is reproduced from Isenrich et al. (2022). Each symbol type represents a different concentration, and different symbol sizes represent independent populations of monodisperse droplets with diameters of approximately 75 μm cooled at 1 K min^{-1} (temperature uncertainty is 0.2 K (Isenrich et al., 2022)). The dash-dotted lines are predictions (not fits) of frozen fractions calculated using Eq. (4) with inputs of each pure mineral's nucleation site density vs. temperature shown in **Fig. 3** assuming an ATD composition of 29 wt.% microcline, 23 wt.% quartz, and 25 wt.% montmorillonite. The corresponding number of nucleation sites per unit surface area, n_s, is plotted as a function of temperature according to Eq. (1) from the experimental frozen fractions using a specific surface area of 22 m^2/g, as reported by for particles between 5 and 10 μm by Ibrahim et al. (2018). For comparison, experimental data of n_s are plotted (lines) and labeled as: W15 digitized from Wheeler et al. (2015); and H14 digitized from Hader et al. (2014) (data labeled unfiltered). The shaded grey area at the lowest temperatures highlights the region where the homogeneous nucleation of pure water in 75 μm droplets occurs; n_s values are thus not plotted in this region.

The median freezing temperatures at each concentration are in the same range as those that would be expected for the fraction of microcline present. If we assume the composition of ATD to be that reported by Kaufmann et al. (2016) (i.e., 29 wt.% microcline, 23 wt.% quartz, and 25 wt.% montmorillonite), we obtain the predictions of frozen fraction shown by the dash-dotted lines for each concentration of ATD in **Fig. 8** using Eq. (4) with the fits obtained from each pure mineral's nucleation site density (shown in **Fig. 3**). There is general agreement between the experimental frozen fractions for ATD and the predicted frozen fractions obtained from the activity of the pure components. This agreement suggests that samples mixed from the pure components can explain the ice nucleation activity of samples that were collected as mixtures from the air or ground, such as ATD. Such an observation can

inform future work in: (*i*) the design of experimental campaigns with controlled bottom-up mineral mixtures acting as surrogates of real field samples without their variability and complexity, and (*ii*) the development of composition-aware parameterizations for ice nucleation in the atmosphere.

4   Conclusions

This work provides a systematic investigation of the ice-nucleation behavior of single minerals and their binary mixtures suspended in varying proportions in microfluidic droplets. The monodispersity and large number of microfluidic droplets in a single experiment provide an important benefit in ensuring the reliable statistical interpretation of results. To process the images obtained from each experiment, a neural network MINCZ-Net was developed to accelerate image processing followed by expert confirmation. One challenge of the microfluidic technique is that pre-processing of the mineral sample was needed to prevent microfluidic channel clogging and to ensure a more homogeneous distribution of particle sizes in the generated droplets. Herein, we filtered all single minerals, and filtration of the montmorillonite was especially challenging due to its swelling behavior. Therefore, such a microfluidic approach is likely better suited for investigating aerosol particles that are inherently smaller via collection by filters or with impactors. Soil samples or crushed mineral samples may have a larger share of supermicron particles that may settle in the tubing or in the microfluidic device, and pre-processing may lead to the exclusion of ice-active material.

A comparison of the active site density of the single mineral microcline to literature results showed a bias towards lower densities, and this difference may be due to the filtration exposing a size-dependence in the ice-nucleation activity (either in the number of sites or their activity). Alternatively, the difference may be accounted for by inherent differences in activity between mineral samples in the literature depending on their source, purity, and processing (e.g., by milling). For the studied binary mixtures, the observed freezing behavior generally followed that of the single most ice-active mineral, and this can be explained by the fact that the minerals are internally mixed within each droplet. Finally, the freezing behavior of Arizona Test Dust (ultrafine fraction) also followed its mineralogical composition (i.e., similar to that of the investigated pure microcline), while its active site density was biased to lower values than those reported in literature, possibly due to uncertainties in the specific surface area or due to inherently different sample-to-sample activity.

This systematic study of three common atmospheric mineral types (microcline, quartz, and montmorillonite) over a wide range of compositions and binary mixture combinations will provide useful input for the design of aerosol- and composition-aware parameterizations of ice nucleation in the presence of multi-mineral particles in the atmosphere. Future work using the microfluidic instrument could investigate the impact of particle size on ice-nucleation activity, other mixtures beyond mineral

1   dusts (e.g., of biological origin), or the effect of solutes in a mixture, while fine-tuning of CNN-

2   supported image processing could lead to rapid analysis of experimental data.

1 **Appendix A1: XRD analysis and DVS isotherms**

2 The composition and purity of natural microcline and montmorillonite were determined using Powder

3 X-ray diffraction (XRD). To this end, approximately 1–3 mg of finely-ground sample powders was

4 loaded on a low-background single-crystal silicon holder. Powder XRD measurements were conducted

5 using an Empyrean 3 diffractometer (Malvern Panalytical) equipped with a Cu source (Cu Kα = 1.5406

6 A, 40 kV, 40 mA) and secondary graphite monochromator at the Institute of Geochemistry and

7 Petrology, Department of Earth and Planetary Sciences, ETH Zurich. The diffraction patterns were

8 continuously collected from 5 to 90° (2θ) with a step size of 0.013° and a 65 s dwell time at ambient

9 temperature using a PIXcel1D detector. Phase identification and Rietveld refinements were carried out

10 using HighScore software and the Crystallography Open Database (COD) to identify the mineralogy

11 and estimate modal abundances. The XRD spectrum for the microcline sample is shown in **Fig. A1**.
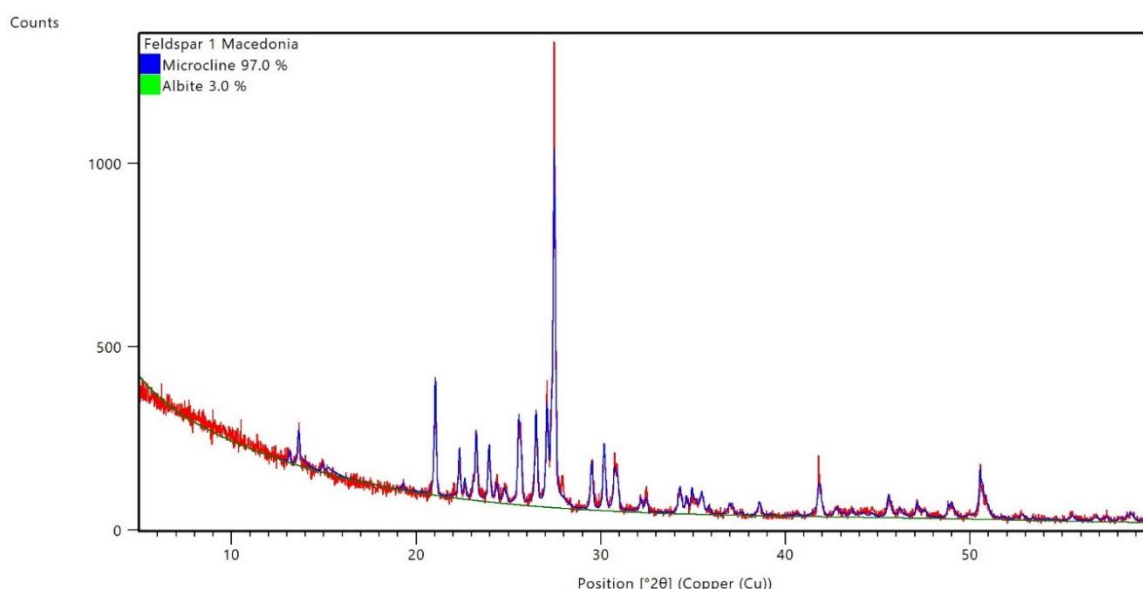
13 **Figure A1**. XRD spectrum of the unprocessed microcline sample from Macedonia obtained from the ETH Mineralogical

14 and Petrographical Collection.

16 **Figure A2** shows the adsorption isotherm for each pure mineral using dynamic vapor sorption (DVS).
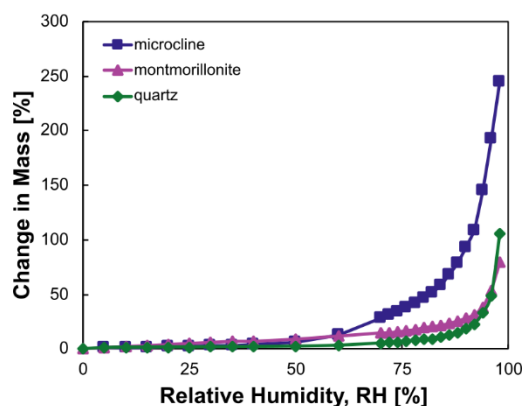
18 **Figure A2**. Adsorption isotherms from dynamic vapor sorption (DVS) measurements for each pure mineral: microcline,

19 montmorillonite, and quartz.

  Appendix A2: Statistical analysis

2 A summary of all experiments reported in the main text is shown in **Fig. A3**, and the corresponding

3 statistical analysis of each pairwise comparison is reported in **Table A1**.
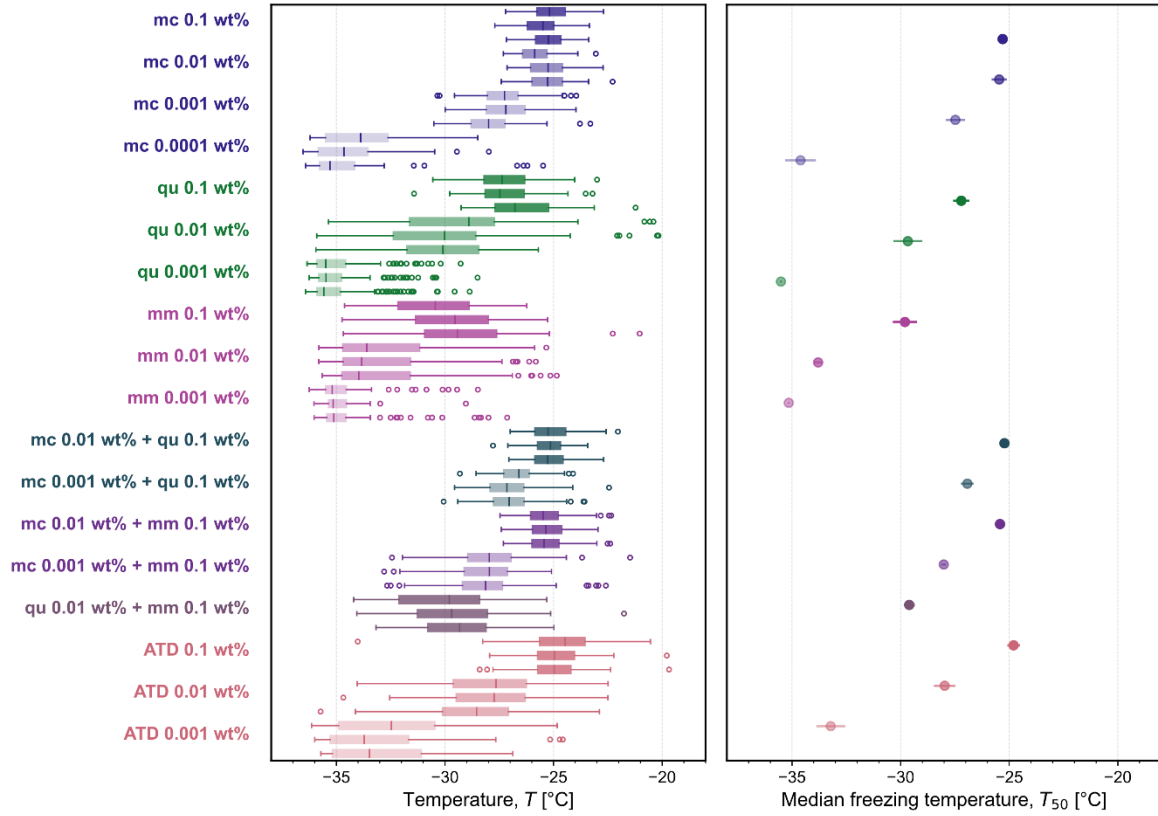
5 **Figure A3.** Box plots of the freezing temperatures for each experiment containing microcline (mc), quartz (qu),

6 montmorillonite (mm), and Arizona Test Dust (ATD) and the corresponding average median temperature T_{50} for each set of

7 three experiments (error bars show one standard deviation). In each box plot, the vertical line indicates the median freezing

8 temperature, the upper and lower bounds of the box stretch across the 25th to 75th percentiles, whiskers span the maximum

9 and minimum temperatures, and open circles are outliers beyond 1.5 times the interquartile range.

11 **Table A1.** Statistical comparison between the median freezing temperatures (T_{50}) of each single mineral and binary mixture

12 studied shown in **Fig. A3**. Differences are tested using Welch's unequal variances t-test and classified into the following

13 categories: not significant (ns), $p \le 0.05$ (*), $p \le 0.01$ (**), and $p \le 0.001$ (***).

	mc 0.01 wt.%	mc 0.001 wt.%	qu 0.1 wt.%	qu 0.01 wt.%	mm 0.1 wt.%	mc 0.01 wt.% + qu 0.1 wt.%	mc 0.001 wt.% + qu 0.1 wt.%	mc 0.01 wt.% + mm 0.1 wt.%	mc 0.001 wt.% + mm 0.1 wt.%	qu 0.01 wt.% + mm 0.1 wt.%
mc 0.01 wt.%										
mc 0.001 wt.%	**									
qu 0.1 wt.%	**	ns								
qu 0.01 wt.%	***	**	**							
mm 0.1 wt.%	***	**	**	ns						
mc 0.01 wt.% + qu 0.1 wt.%	ns	***	***	***	***					
mc 0.001 wt.% + qu 0.1 wt.%	**	ns	ns	**	**	***				
mc 0.01 wt.% + mm 0.1 wt.%	ns	**	**	***	***	*	***			
mc 0.001 wt.% + mm 0.1 wt.%	***	ns	*	*	**	***	**	***		
qu 0.01 wt.% + mm 0.1 wt.%	***	**	***	ns	ns	***	***	***	***	

Code and data availability

Plot data are compiled in the ETH Research Collection data repository at https://doi.org/10.3929/ethz-b-000736892 [*link will be activated prior to final submission*]. Python scripts are available upon request.

Author contribution

NS contributed to project conceptualization, methodology, experimental measurements, software development, data analysis and interpretation, and writing (first draft). FNI contributed to the design of the microfluidic devices, methodology, sample preparation, and data interpretation. JN contributed to SEM analysis; CD to DVS measurements; and NM to XRD analysis. CM and ZAK contributed to project conceptualization, methodology development, and data interpretation. All authors contributed to writing (review and editing) and have approved the final version of the manuscript.

Competing interests

The authors declare that they have no conflict of interest.

Acknowledgements

We acknowledge Roland Walker and Michael Rösch for technical support with hardware upgrades to the instrument; Andrea Galli for providing the microcline sample from the ETH Mineralogical and Petrographical Collection and for helpful discussions; Lydia Zehnder for milling the microcline sample; Imad El-Bakouri for assisting with making microfluidic devices and for motivating both hardware and software upgrades to the instrument; Evdokia Saiti for assistance with image registration and visualizing the CNN in Fig. 1; Kristian Klumpp and Thomas Peter for enthusiastic discussions and interest in the setup and results; Ulrike Lohmann for hosting the project and providing infrastructure and support; and the anonymous reviewers for their suggestions that improved the quality of this manuscript.

Financial support

NS acknowledges support from an ETH Postdoctoral Fellowship (20-1 FEL-46).

References

Alpert, P. A. and Knopf, D. A.: Analysis of isothermal and cooling-rate-dependent immersion freezing by a unifying stochastic ice nucleation model, Atmospheric Chemistry and Physics, 16, 2083-2107, 10.5194/acp-16-2083-2016, 2016.

Atkinson, J. D., Murray, B. J., Woodhouse, M. T., Whale, T. F., Baustian, K. J., Carslaw, K. S., Dobbie, S., O'Sullivan, D., and Malkin, T. L.: The importance of feldspar for ice nucleation by mineral dust in mixed-phase clouds, Nature, 498, 355-358, 10.1038/nature12278, 2013.

Beall, C. M., Hill, T. C. J., DeMott, P. J., Köneman, T., Pikridas, M., Drewnick, F., Harder, H., Pöhlker, C., Lelieveld, J., Weber, B., Iakovides, M., Prokeš, R., Sciare, J., Andreae, M. O., Stokes, M. D., and Prather, K. A.: Ice-nucleating particles near two major dust source regions, Atmospheric Chemistry and Physics, 22, 12607-12627, 10.5194/acp-22-12607-2022, 2022.

Bergeron, T.: On the physics of clouds and precipitation, in: Proces Verbaux de l'Association de Météorologie, International Union of Geodesy and Geophysics, 156–178, 1935.

Blattmann, T. M. and Plötze, M.: BET-based mineral surface area quantification comparing nitrogen with water, Applied Clay Science, 258, 10.1016/j.clay.2024.107477, 2024.

Broadley, S. L., Murray, B. J., Herbert, R. J., Atkinson, J. D., Dobbie, S., Malkin, T. L., Condliffe, E., and Neve, L.: Immersion mode heterogeneous ice nucleation by an illite rich powder representative of atmospheric mineral dust, Atmospheric Chemistry and Physics, 12, 287-307, 10.5194/acp-12-287-2012, 2012.

Burrows, S. M., McCluskey, C. S., Cornwell, G., Steinke, I., Zhang, K., Zhao, B., Zawadowicz, M., Raman, A., Kulkarni, G., China, S., Zelenyuk, A., and DeMott, P. J.: Ice-Nucleating Particles That Impact Clouds and Climate: Observational and Modeling Research Needs, Reviews of Geophysics, 60, 10.1029/2021rg000745, 2022.

Chatziparaschos, M., Daskalakis, N., Myriokefalitakis, S., Kalivitis, N., Nenes, A., Gonçalves Ageitos, M., Costa-Surós, M., Pérez García-Pando, C., Zanoli, M., Vrekoussis, M., and Kanakidou, M.: Role of K-feldspar and quartz in global ice nucleation by mineral dust in mixed-phase clouds, Atmospheric Chemistry and Physics, 23, 1785-1801, 10.5194/acp-23-1785-2023, 2023.

Deck, L. T., Shardt, N., El-Bakouri, I., Isenrich, F. N., Marcolli, C., deMello, A. J., and Mazzotti, M.: Monitoring Aqueous Sucrose Solutions Using Droplet Microfluidics: Ice Nucleation, Growth, Glass Transition, and Melting, Langmuir, 40, 6304-6316, 10.1021/acs.langmuir.3c03798, 2024.

Dogan, M., Dogan, A. U., Yesilyurt, F. I., Alaygut, D., Buckner, I., and Wurster, D. E.: Baseline studies of the Clay Minerals Society special clays: Specific surface area by the Brunauer Emmett Teller (BET) method, Clays and Clay Minerals, 55, 534-541, 10.1346/ccmn.2007.0550508, 2007.

Findeisen, W.: Die kolloidmeteorologischen Vorgänge bei der Niederschlagsbildung (Colloidal meteorological processes in the formation of precipitation), Meteorologische Zeitschrift, 55, 121-133, 10.1127/metz/2015/0675, 1938.

Gronquist, P., Frey, M., Keplinger, T., and Burgert, I.: Mesoporosity of Delignified Wood Investigated by Water Vapor Sorption, ACS Omega, 4, 12425-12431, 10.1021/acsomega.9b00862, 2019.

Hader, J. D., Wright, T. P., and Petters, M. D.: Contribution of pollen to atmospheric ice nuclei concentrations, Atmospheric Chemistry and Physics, 14, 5433-5449, 10.5194/acp-14-5433-2014, 2014.

Hamzehpour, N., Marcolli, C., Klumpp, K., Thöny, D., and Peter, T.: The Urmia playa as a source of airborne dust and ice-nucleating particles – Part 2: Unraveling the relationship between soil dust

composition and ice nucleation activity, Atmospheric Chemistry and Physics, 22, 14931-14956, 10.5194/acp-22-14931-2022, 2022.

Harrison, A. D., Lever, K., Sanchez-Marroquin, A., Holden, M. A., Whale, T. F., Tarn, M. D., McQuaid, J. B., and Murray, B. J.: The ice-nucleating ability of quartz immersed in water and its atmospheric importance compared to K-feldspar, Atmospheric Chemistry and Physics, 19, 11343-11361, 10.5194/acp-19-11343-2019, 2019.

Harrison, A. D., Whale, T. F., Carpenter, M. A., Holden, M. A., Neve, L., O'Sullivan, D., Vergara Temprado, J., and Murray, B. J.: Not all feldspars are equal: a survey of ice nucleating properties across the feldspar group of minerals, Atmospheric Chemistry and Physics, 16, 10927-10940, 10.5194/acp-16-10927-2016, 2016.

Hoose, C. and Möhler, O.: Heterogeneous ice nucleation on atmospheric aerosols: a review of results from laboratory experiments, Atmospheric Chemistry and Physics, 12, 9817-9854, 10.5194/acp-12-9817-2012, 2012.

House, M. L. and Dutcher, C. S.: Microfluidic enabled ice nucleation studies of montmorillonite clay at varying pH and ionic strengths with refreezing and relative humidity cycling, Aerosol Science and Technology, 58, 1168-1181, 10.1080/02786826.2024.2371412, 2024.

Ibrahim, S., Romanias, M. N., Alleman, L. Y., Zeineddine, M. N., Angeli, G. K., Trikalitis, P. N., and Thevenet, F.: Water Interaction with Mineral Dust Aerosol: Particle Size and Hygroscopic Properties of Dust, ACS Earth and Space Chemistry, 2, 376-386, 10.1021/acsearthspacechem.7b00152, 2018.

Isenrich, F. N., Shardt, N., Rösch, M., Nette, J., Stavrakis, S., Marcolli, C., Kanji, Z. A., deMello, A. J., and Lohmann, U.: The Microfluidic Ice Nuclei Counter Zürich (MINCZ): a platform for homogeneous and heterogeneous ice nucleation, Atmospheric Measurement Techniques, 15, 5367-5381, 10.5194/amt-15-5367-2022, 2022.

Kanji, Z. A., Ladino, L. A., Wex, H., Boose, Y., Burkert-Kohn, M., Cziczo, D. J., and Krämer, M.: Overview of Ice Nucleating Particles, Meteorological Monographs, 58, 1.1-1.33, 10.1175/amsmonographs-d-16-0006.1, 2017.

Kaufmann, L., Marcolli, C., Hofer, J., Pinti, V., Hoyle, C. R., and Peter, T.: Ice nucleation efficiency of natural dust samples in the immersion mode, Atmospheric Chemistry and Physics, 16, 11177-11206, 10.5194/acp-16-11177-2016, 2016.

Klumpp, K., Marcolli, C., and Peter, T.: The impact of (bio-)organic substances on the ice nucleation activity of the K-feldspar microcline in aqueous solutions, Atmospheric Chemistry and Physics, 22, 3655-3673, 10.5194/acp-22-3655-2022, 2022.

Klumpp, K., Marcolli, C., Alonso-Hellweg, A., Dreimol, C. H., and Peter, T.: Comparing the ice nucleation properties of the kaolin minerals kaolinite and halloysite, Atmospheric Chemistry and Physics, 23, 1579-1598, 10.5194/acp-23-1579-2023, 2023.

Knopf, D. A. and Alpert, P. A.: Atmospheric ice nucleation, Nature Reviews Physics, 5, 203-217, https://doi.org/10.1038/s42254-023-00570-7, 2023.

Kok, J. F., Storelvmo, T., Karydis, V. A., Adebiyi, A. A., Mahowald, N. M., Evan, A. T., He, C., and Leung, D. M.: Mineral dust aerosol impacts on global climate and climate change, Nature Reviews Earth & Environment, 4, 71-86, 10.1038/s43017-022-00379-5, 2023.

Kumar, A., Marcolli, C., Luo, B., and Peter, T.: Ice nucleation activity of silicates and aluminosilicates in pure water and aqueous solutions – Part 1: The K-feldspar microcline, Atmospheric Chemistry and Physics, 18, 7057-7079, 10.5194/acp-18-7057-2018, 2018.

Kumar, A., Klumpp, K., Barak, C., Rytwo, G., Plötze, M., Peter, T., and Marcolli, C.: Ice nucleation by smectites: the role of the edges, Atmospheric Chemistry and Physics, 23, 4881-4902, 10.5194/acp-23-4881-2023, 2023.

Lacher, L., Lohmann, U., Boose, Y., Zipori, A., Herrmann, E., Bukowiecki, N., Steinbacher, M., and Kanji, Z. A.: The Horizontal Ice Nucleation Chamber (HINC): INP measurements at conditions relevant for mixed-phase clouds at the High Altitude Research Station Jungfraujoch, Atmospheric Chemistry and Physics, 17, 15199-15224, 10.5194/acp-17-15199-2017, 2017.

Mahrt, F., Rösch, C., Gao, K., Dreimol, C. H., Zawadowicz, M. A., and Kanji, Z. A.: Physicochemical properties of charcoal aerosols derived from biomass pyrolysis affect their ice-nucleating abilities at cirrus and mixed-phase cloud conditions, Atmospheric Chemistry and Physics, 23, 1285-1308, 10.5194/acp-23-1285-2023, 2023.

Miller, A. J., Brennan, K. P., Mignani, C., Wieder, J., David, R. O., and Borduas-Dedekind, N.: Development of the drop Freezing Ice Nuclei Counter (FINC), intercomparison of droplet freezing techniques, and use of soluble lignin as an atmospheric ice nucleation standard, Atmospheric Measurement Techniques, 14, 3131-3151, 10.5194/amt-14-3131-2021, 2021.

Murray, B. J., O'Sullivan, D., Atkinson, J. D., and Webb, M. E.: Ice nucleation by particles immersed in supercooled cloud droplets, Chem Soc Rev, 41, 6519-6554, 10.1039/c2cs35200a, 2012.

Peckhaus, A., Kiselev, A., Hiron, T., Ebert, M., and Leisner, T.: A comparative study of K-rich and Na/Ca-rich feldspar ice-nucleating particles in a nanoliter droplet freezing assay, Atmospheric Chemistry and Physics, 16, 11477-11496, 10.5194/acp-16-11477-2016, 2016.

Pinti, V., Marcolli, C., Zobrist, B., Hoyle, C. R., and Peter, T.: Ice nucleation efficiency of clay minerals in the immersion mode, Atmospheric Chemistry and Physics, 12, 5859-5878, 10.5194/acp-12-5859-2012, 2012.

Polen, M., Brubaker, T., Somers, J., and Sullivan, R. C.: Cleaning up our water: reducing interferences from nonhomogeneous freezing of "pure" water in droplet freezing assays of ice-nucleating particles, Atmospheric Measurement Techniques, 11, 5315-5334, 10.5194/amt-11-5315-2018, 2018.

Reicher, N., Segev, L., and Rudich, Y.: The WeIzmann Supercooled Droplets Observation on a Microarray (WISDOM) and application for ambient dust, Atmospheric Measurement Techniques, 11, 233-248, 10.5194/amt-11-233-2018, 2018.

Rogers, D. C.: Development of a continuous flow thermal gradient diffusion chamber for ice nucleation studies, Atmospheric Research, 22, 149-181, 1988.

Rogers, D. C., DeMott, P. J., Kreidenweis, S. M., and Chen, Y.: A Continuous-Flow Diffusion Chamber for Airborne Measurements of Ice Nuclei, Journal of Atmospheric and Oceanic Technology, 18, 725-741, 2001.

Tarn, M. D., Sikora, S. N. F., Porter, G. C. E., O'Sullivan, D., Adams, M., Whale, T. F., Harrison, A. D., Vergara-Temprado, J., Wilson, T. W., Shim, J. U., and Murray, B. J.: The study of atmospheric ice-nucleating particles via microfluidically generated droplets, Microfluid Nanofluidics, 22, 52, 10.1007/s10404-018-2069-x, 2018.

Vali, G.: Interpretation of freezing nucleation experiments: singular and stochastic; sites and surfaces, Atmospheric Chemistry and Physics, 14, 5271-5294, 10.5194/acp-14-5271-2014, 2014.

Vali, G., DeMott, P. J., Möhler, O., and Whale, T. F.: Technical Note: A proposal for ice nucleation terminology, Atmospheric Chemistry and Physics, 15, 10263-10270, 10.5194/acp-15-10263-2015, 2015.

Wegener, A.: Thermodynamik der atmosphäre, Johann Ambrosius Barth, Leipzig 1911.

Whale, T. F., Holden, M. A., Wilson, T. W., O'Sullivan, D., and Murray, B. J.: The enhancement and suppression of immersion mode heterogeneous ice-nucleation by solutes, Chem Sci, 9, 4142-4151, 10.1039/c7sc05421a, 2018.

Whale, T. F., Holden, M. A., Kulak, A. N., Kim, Y. Y., Meldrum, F. C., Christenson, H. K., and Murray, B. J.: The role of phase separation and related topography in the exceptional ice-nucleating ability of alkali feldspars, Phys Chem Chem Phys, 19, 31186-31193, 10.1039/c7cp04898j, 2017.

Wheeler, M. J., Mason, R. H., Steunenberg, K., Wagstaff, M., Chou, C., and Bertram, A. K.: Immersion freezing of supermicron mineral dust particles: freezing results, testing different schemes for describing ice nucleation, and ice nucleation active site densities, J Phys Chem A, 119, 4358-4372, 10.1021/jp507875q, 2015.

Wong, B.: The Impact of Mixed Mineral Dust Particle Populations on Atmospheric Ice Nucleation, Stony Brook University, 2019.

Wright, T. P. and Petters, M. D.: The role of time in heterogeneous freezing nucleation, Journal of Geophysical Research: Atmospheres, 118, 3731-3743, 10.1002/jgrd.50365, 2013.

Yun, J., Kumar, A., Removski, N., Shchukarev, A., Link, N., Boily, J.-F., and Bertram, A. K.: Effects of Inorganic Acids and Organic Solutes on the Ice Nucleating Ability and Surface Properties of Potassium-Rich Feldspar, ACS Earth and Space Chemistry, 5, 1212-1222, 10.1021/acsearthspacechem.1c00034, 2021.

Yun, J., Link, N., Kumar, A., Shchukarev, A., Davidson, J., Lam, A., Walters, C., Xi, Y., Boily, J.-F., and Bertram, A. K.: Surface Composition Dependence on the Ice Nucleating Ability of Potassium-Rich Feldspar, ACS Earth and Space Chemistry, 4, 873-881, 10.1021/acsearthspacechem.0c00077, 2020.

Zolles, T., Burkart, J., Hausler, T., Pummer, B., Hitzenberger, R., and Grothe, H.: Identification of ice nucleation active sites on feldspar dust particles, J Phys Chem A, 119, 2692-2700, 10.1021/jp509839x, 2015.